Heterogeneous Motion of Secretory Vesicles in the Actin Cortex of Live Cells: 3D Tracking to 5-nm Accuracy†

Michael C. Konopka and James C. Weisshaar*

Department of Chemistry, University of Wisconsin—Madison, Madison, Wisconsin 53706

Received: April 27, 2004; In Final Form: August 18, 2004

Fluorescence microscopy tracks the three-dimensional motion of green fluorescent protein (GFP)-labeled large dense-core secretory vesicles (LDCVs) within the actin cortex of live PC12 cells. In this study, we achieve a 26-ms time resolution and a spatial accuracy of 5 nm or better in each dimension (one standard deviation in one dimension, σ_{1D}). The resulting high-resolution trajectories reveal not only heterogeneity among vesicles but also heterogeneity within single-vesicle trajectories. As in earlier work, we observe three apparent groups of vesicles: the immobile, mobile, and directed-motion groups, but the distinctions among the groups are blurred. The directed trajectories exhibit segments with kinesin-like speed punctuated by pauses and changes in speed and direction. The immobile vesicles nearest the plasma membrane jump among sub-25-nm-diameter "mini-traps". Comparison with microrheological data from entangled F-actin solutions suggests that the jumps may be caused by local remodeling of F-actin. Motion within a mini-trap is quantitatively modeled by a random walk in a parabolic restoring potential to yield single-trap restoring force constants of ∼0.04 pN/nm. As judged by mean-square displacement versus time, the mobile vesicles execute nearly free random walks in an elastic medium. We find no clear evidence of quasi-linear, directed motion in the mobile group. However, heterogeneity is evident in the distribution of frame-to-frame displacements, $P(r)$, which requires a two-component fit. Evidently, mobile vesicles move by a combination of diffusion and motor-driven motion, with the direction changing rapidly as myosin-V crisscrosses the dense F-actin meshwork. The frequency of long frame-to-frame displacements of 25−70 nm suggests the presence of one or more myosin-V motors on the mobile vesicles. We argue that the motors on the immobile vesicles are less active or completely inactive. This suggests a regulatory mechanism for motor activity that may be related to the cell's ability to mobilize vesicles upon stimulation by Ca^{2+}.

Introduction

In neuroendocrine cells (Figure 1), secretory vesicles carry neuropeptides and hormones from the trans-Golgi network (TGN) through the actin cortex to the plasma membrane (PM).[1] These 100−200-nm-diameter vesicles dock at the PM and await cell depolarization and the sudden influx of Ca^{2+} that triggers exocytosis, the rapid release of the vesicle contents to the extracellular medium. This tightly regulated process controls the delivery of chemical signals throughout the nervous and endocrine systems. In the late stages of transport to the PM, the vesicle must traverse the actin cortex, a viscoelastic medium comprising actin filaments in a dense, cross-linked network ∼0.5−1.0 μm thick with a mesh size of ∼50 nm.[2] Motion through the cortex may involve a combination of *passive transport*, meaning Brownian motion in a time-varying field of filamentous and other barriers, and *active transport*, which could involve the propulsion of vesicles by actin polymerization or the pulling of vesicles along microtubules (MTs) and actin filaments by kinesin and myosin motor proteins.[3−5] In resting cells, vesicles establish a steady-state concentration distribution strongly peaked in the actin cortex near the PM, which suggests binding between the vesicles and the cortex. It is largely an open question what specific factors establish this spatial distribution and allow it to respond to stimulation and exocytosis.

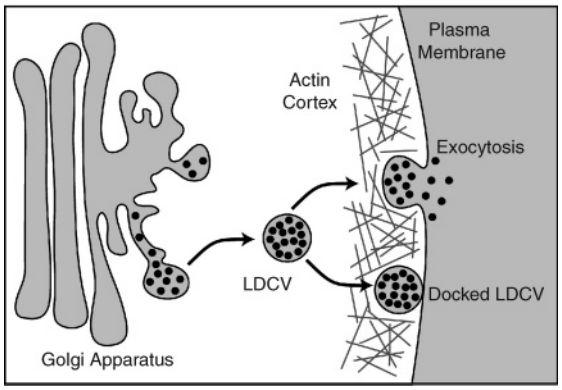

Figure 1. Schematic of a PC12 cell showing the trans-Golgi network, where large dense-core secretory vesicles (LDCVs) are formed; the actin cortex; and the plasma membrane, where LDCVs dock and carry out Ca^{2+}-triggered exocytosis.

Different types of cells may use different combinations of transport and binding mechanisms.[6] An elegant series of studies has shown that melanosome trafficking in mouse melanocytes is controlled by *three types* of motor proteins.[4,7−9] Kinesin and dynein motors enable fast, bidirectional motion between the TGN and the PM on microtubule filaments. Within the actin cortex, myosin-Va is involved at least in the binding of melanosomes (the *capture model*). In rat pheochromocytoma (PC12) cells, recent work provided strong biochemical evidence that at least half of the large dense-core secretory vesicles

† Part of the special issue "Tomas Baer Festschrift".

* Corresponding author. E-mail: weisshaar@chem.wisc.edu.

10.1021/jp048162v CCC: $27.50
Published on Web 10/07/2004

(LDCVs) carry myosin-Va motors.[10] In addition, the same LDCVs exhibit fast, seemingly unidirectional motion from the TGN to the PM at speeds characteristic of kinesin motors. Within the actin cortex, the coarse motion was characterized as random movement. As for melanosomes, the expression of a dominant negative tail domain of myosin-Va depleted the number of LDCVs in the actin cortex.[11] The faster components of the speed distribution were also depleted. Related earlier studies of the motion of green fluorescent protein (GFP)-labeled LDCVs in PC12 cells[5,12] found that LDCV motion stopped when the remodeling of F-actin was prevented by the addition of phalloidin or the withdrawal of MgATP. Motion also slowed when the cortex was degraded by latrunculin. These results suggest that cortical actin filaments hinder vesicle motion by acting as a physical barrier but also mediate the motion.

Several groups[13−17] have used total internal reflectance fluorescence microscopy (TIRFM) to track secretory vesicles in the actin cortex of live chromaffin and PC12 cells. The time and spatial resolution have typically been about 0.5 s and 50 nm. In chromaffin cells, Oheim and co-workers achieved ∼15−20-nm lateral and 5-nm axial accuracy (one standard deviation in each dimension, σ_{1D}).[18] Here, we use TIRFM to track LDCVs that carry a neuropeptide−GFP fusion protein within undifferentiated PC12 cells. Owing to the high S/N ratio, a fast camera, and Gaussian fitting of the *xy* images, we can track the centers of bright vesicles with $\sigma_{1D} = 5$ nm or less in *x*, *y*, and *z* with a 26-ms time resolution. The resulting high-resolution vesicle trajectories reveal new levels of detail in vesicle motion. As in previous work,[5,18−21] plots of single-vesicle mean-square displacement versus time suggest three groups of vesicles: an *immobile group* which undergoes diffusive motion within confinements or among barriers or obstacles; a *mobile group* which carries out more nearly field-free diffusion without confinement; and a small subset of vesicles that clearly undergo *directed motion*, evidently driven by the motor protein kinesin and perhaps by myosin-V as well. This is heterogeneity *among vesicles*. Our temporal and spatial resolution are capable of resolving individual myosin-Va steps and dwells between steps. Within the mobile and immobile groups, the distribution of one-step frame-to-frame displacements, $P(r)$, reveals fast and slow modes of motion on the 26-ms time scale. We interpret these as arising from periods of myosin-Va activity and inactivity.

The high-resolution trajectories further blur the distinctions among mobile, immobile, and directed-motion vesicles by revealing states of motion that *change in time* for a single vesicle. This is heterogeneity *within single trajectories*. Many vesicles change character from immobile to mobile or from directed to mobile; some change speed and stop and start. The time-correlation function of $r^2(t)$, the squared displacement versus time, reveals heterogeneity in a subset of individual trajectories on two different time scales, 0−0.1 s and 0−5 s. In addition, the immobile vesicles nearest the PM migrate among a series of "mini-traps" with diameters on the order of 50 nm or less. We analyze the motion within mini-traps by comparison to confined random walk models. The data are well fit by random walks with a central restoring force ("elastic traps") but not by simple random walks within a confining sphere. We find heterogeneity in the diffusion coefficient and force constant of the elastic traps that correlates with the apparent distance above the plasma membrane. Comparison of these results with microrheological studies of fluorescent microspheres embedded in F-actin solutions suggests that cross-linking and remodeling of the cortex in vivo lead to a characteristic positive curvature in log−log plots of mean-square displacement (MSD) versus τ that is not observed in vitro.

Materials and Methods

Cell Culture. PC-12 cells were obtained from the Martin lab at UW-Madison Biochemistry.[12] These cells are stably transfected to express the neuropeptide−GFP fusion protein ANF−Emd (emerald GFP) within undifferentiated PC12 cells. ANF−Emd is brighter than ANF−EGFP. Cells were cultured at 37 °C in a humidified atmosphere of 10% CO_2 in 100-mm dishes in Dulbecco's modified Eagle's medium (DMEM), with 4.5 mg/mL glucose, 3.7 mg/mL $NaHCO_3$, 5% horse serum, and 5% iron-supplemented calf serum. One day prior to experiments, cells were plated on Mattek 35-mm glass-bottom culture dishes precoated with 50 μg of collagen I and poly-D-lysine. To obtain isolated single cells for study, cells were plated at a density of 1×10^4 cells/cm^2 in a Petri dish. Prior to the experiment, the culture medium is replaced with an incubation buffer of 150 mM NaCl, 4.2 mM KCl, 1 mM NaH_2PO_4, 0.7 mM $MgCl_2$, 10 mM *N*-(2-hydroxyethyl)piperazine-*N*′-ethanesulfonic acid (HEPES), and 2 mM $CaCl_2$ (pH 7.4). All experiments are performed at 25 °C. The cells chosen for study were single cells of intermediate brightness, which optimizes the ability to track individual vesicles accurately for long periods of time.

Microscopy: High-Resolution Trajectories. In TIRFM, a continuous-wave laser beam illuminates a thin slab some 200 nm thick at the base of live cells adhered to a coverslip.[14,21,22] We use through-the-objective TIR with an Olympus 60×, 1.45 NA objective adapted to an inverted Nikon microscope (resulting magnification, 66.7×). An Ar^+ laser intensity of 0.65 mW at 488 nm is focused to an elliptical spot size of 11 μm × 18 μm full width at half-maximum (fwhm) at the glass−cell interface. Fluorescence was isolated using a 495-nm long-pass dichroic mirror and a 20-nm band-pass filter centered at 520 nm to limit cell autofluorescence. Widefield two-dimensional movies in the *xy* plane are recorded with a fast charge-coupled device (CCD) camera (CoolSnap HQ, 1392 × 1040 pixels, 6.45 μm pixels corresponding to 97 nm at the sample). A full cell image typically fits in a region of interest of about 100 × 100 pixels, enabling a frame duration of $\Delta t = 26.2$ ms (frame rate, 38.2 Hz). The density of readily observed vesicles is typically 1.0 μm^{-2}; the vesicles under study vary by about a factor of 5 in intensity within a typical cell. Increasing laser intensity increases the S/N ratio but shortens the useful duration of a movie due to photobleaching. We have obtained high quality movies for 500 frames (12.5 s).

After the filtering of the images in Fourier space (0.5-μm^{-1} high-pass filter), a computer tracking algorithm written in the interactive data language extracts 3D trajectories from the time sequence of images. We accept only those trajectories that last at least 20 frames while suffering no "fusion" or "fission" events (see below). First, each *xy* spot in each frame is fit to a 2D Gaussian function on a 7 × 7 pixel grid using nonlinear least squares with all pixels equally weighted. The fitting parameters include the center position (x_0, y_0), the peak intensity, the angle of rotation of the Gaussian coordinates relative to the pixel coordinates, the independent full width at half-maximum (fwhm) parameters along the two Gaussian axes, and the local baseline amplitude. For spatially well resolved vesicles, the Gaussian fits are statistically good and have consistent fwhm's of 217 ± 10 nm (one standard deviation) along both *x* and *y*, strongly suggesting we are tracking single vesicles.

We use the time-dependent total intensity to calculate a *relative z* position from the exponential decay of laser intensity

along z, $I = I_0 \exp(-z/z_0)$. Here, I_0 is the intensity at the glass−cell interface (where $z = 0$) and z_0 depends on the laser angle of incidence and wavelength as well as the refractive index of glass and of the cell. We measure the angle of incidence as $70 \pm 1°$ (close to the limit of 72° for the 1.45 NA objective) and estimate the effective refractive index for the cell as 1.365 ± 0.015[18] to obtain the estimate $z_0 = 90 \pm 10$ nm. To assess the extent of photobleaching, we fixed PC12 cells in formaldehyde and measured the approximately exponential decay of fluorescence intensity for stationary single vesicles. The $1/e$ decay times vary from 20 to 80 s. For vesicles that move along z, photobleaching should be multiexponential and is difficult to assess. On a 50-frame time scale, bleaching is unimportant; it should contribute a monotonic drift in apparent z of only 2−6 nm, depending on the vesicle's z trajectory in time. On a 200-frame time scale, the drift corresponds to 6−24 nm. Thus, changes in z on short time scales can be measured with a 4-nm precision, unaffected by bleaching.[21] Comparison of apparent z values between different vesicles can be misleading due to the distribution of intrinsic vesicle brightness (GFP copy number). For the fixed cells, if we assume the *bleach lifetime* faithfully reports the relative z values across different vesicles, then the range of initial intensities for vesicles with similar lifetimes gives information about the range of intrinsic brightnesses. This range is roughly a factor of 2 in our PC12 cells, which corresponds to an error of ∼60 nm or less in comparing apparent z values across vesicles. In chromaffin cells, LDCVs varied by about a factor of 3 in intrinsic brightness.[21]

The algorithm forms trajectories by "connecting the dots" between nearest neighbors in the *xy* plane of successive frames, keeping track of newcomers and of vesicles that leave the field of view. The algorithm ignores pairs of vesicles that lie within 300 nm center-to-center. Since the largest step sizes observed are 70−100 nm, this essentially eliminates difficulties in tracking the same vesicle from frame to frame. Fusion events (coalescence of two vesicles in the *xy* plane vs time) are thus eliminated, and fission events (splitting of two initially coincident vesicles in the *xy* plane into two distinguishable vesicles) are eliminated by visual inspection. For fewer than 1% of the frame-to-frame steps, the goodness-of-fit statistic χ^2 jumps above a threshold that sensitively indicates distortion of the image by a nearby bright vesicle. For these rare frames, both Gaussian and centroid fitting methods fail, so we interpolate positions to avoid distortion of r and r^2 statistics. Our analysis procedure generally discriminates against long, rapidly moving trajectories because they are likely to cross other vesicles. TIRFM necessarily cuts off trajectories that move more than 200−300 nm in z.

The measurement accuracy of the vesicle *xy center position* is limited not by the wavelength of light but by the signal-to-noise ratio, pixel size, instrument vibration and drift, and statistical uniformity of background light.[23,24] To test the theoretical limit on accuracy under our conditions, we used the Gaussian fitting routine to track computer-simulated pixellated images that include shot noise, readout noise, 2D Gaussian widths, and pixel size matched to experiment.[25] As the image S/N ratio averaged over the nine most intense pixels varies from 25 to 15 to mimic the range of most of the tracked vesicles, the root-mean-square (rms) fitting error σ_{1D} (standard deviation along one dimension) increases from 2.5 to 4.5 nm, while the average bias remains below 0.2 nm. A centroid algorithm introduces bias as large as 2 nm. In the actual experimental trajectories, we observe many small "traps", stretches of 20 to 150 frames during which a vesicle is approximately stationary. Such features frequently exhibit σ_{1D} along x, y, or z in the range 4−6 nm. Trajectories that exhibit clear directional motion frequently deviate from a smooth path by <5 nm rms. This is comparable to a recent study of single myosin steps.[23]

Since real trajectories in live cells include genuine thermal motion, we estimate that the one-dimensional measurement uncertainty σ_{1D} is at most 5 nm along each of x, y, and z. The three-dimensional, frame-to-frame displacement of the particle, $r = ((x_2 - x_1)^2 + (y_2 - y_1)^2 + (z_2 - z_1)^2)^{1/2}$, then has variance $\sigma^2(r) = 2\sigma_{1D}^2 < 50$ nm^2, and the squared displacement, r^2, has variance $\sigma^2(r^2) = 8\sigma_{1D}^2 r^2 < 200 r^2$ in nm^4.

Apparatus vibration sometimes appears in movies as a correlated periodic motion of nearby "immobile" vesicles and is most troublesome at low frequencies of 1−3 Hz. The amplitude of such vibration was limited to <3 nm rms. Thermal drift would appear as a correlated translational motion of all vesicles in the *xy* plane but was not in evidence in the reported data. To corroborate the measurement accuracy, we fixed PC12 cells in formaldehyde and tracked the apparent motion of the LDCVs. MSD(τ) levels off after two to three frames at a value of 50−100 nm^2; the variation among vesicles suggest the presence of some real thermal motion. This corresponds to σ_{1D} in the range 4−6 nm, consistent with estimates from the narrowest observed features. In the unfixed cells, even the slow-moving vesicles have one-step MSD($\tau = 0.026$ s) values in the range 250−1000 nm^2, so the measured one-step MSD is dominated by real motion. The time and space resolution are well matched.

Random Walk Models. We have examined three random walk models in three-dimensional space:[26] force-free random walks, characterized by a diffusion coefficient, D; walks constrained to lie within a sphere of radius R_0 with no restoring potential, characterized by R_0 and D; and walks within a central restoring potential of the form $V(R) = {}^1/_2\kappa R^2$, characterized by D and κ. Here, κ is the (positive) restoring force constant and R measures the distance from the center of force. The latter model mimics an elastic medium. In each case, fine-grained steps were generated with $\Delta t = 0.000\,262$ s (one-hundredth of the camera frame time scale) by sampling Δx, Δy, and Δz from a Gaussian distribution whose width determines the short-time diffusion coefficient, D. In all models, coarse-grained walks directly comparable to experiment were obtained by sampling every hundredth position of the fine-grained walks. Results were not distinguishable from those obtained by averaging each one hundred positions to obtain the coarse-grained walk.

For the free walks, we mimic the limited range of z accessible in our experiments by rejecting steps that would move below $z = 0$ nm and terminating a walk if it moves beyond a distance of $z = 250$ nm. Walks begin at random z within that range. For walks within a sphere, the particle begins at the origin; steps that would take the fine-grained walk beyond distance R_0 from the origin are rejected. The results did not depend on the choice of initial position for the 200-step walks of interest. The walks in the restoring potential use Monte Carlo methods to choose steps that generate a canonical distribution of positions at temperature T: $P(R) = AR^2 \exp(-{}^1/_2\kappa R^2/kT)$, with A being a normalization constant, k being the Boltzmann constant, and $T = 300$ K. Particles begin at the center of force. Results were independent of initial position for the 200-step walks of interest.

Results

Overview of Trajectory Types. We have examined some 200 nonoverlapped, high-resolution trajectories of 20−500 frames collected from five representative PC-12 cells. We can

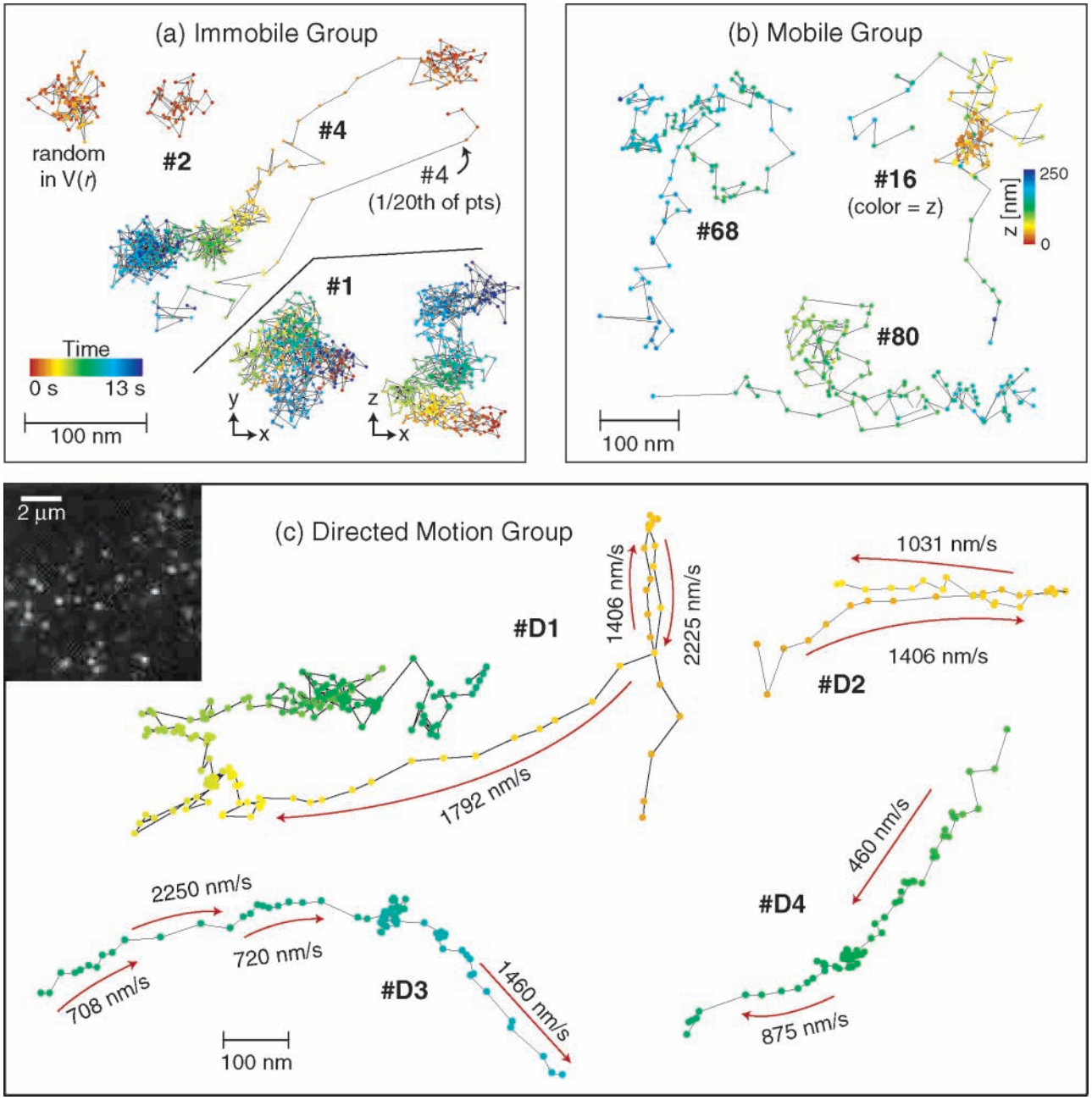

Figure 2. Projections of high-resolution trajectories onto the *xy* plane. Color encodes time except for vesicle #16, for which it encodes *z*. Local speed of directed segments in nanometers per second as indicated. (a) Three immobile trajectories, including two projections of #1 plus one 200-frame trajectory generated by a Monte Carlo random walk in a parabolic restoring potential. (b) Three mobile trajectories. (c) Four directed trajectories. The inset shows an image of a live PC12 cell. Scale bar = 2 μm.

extract 40−50 nonoverlapping trajectories of 20 frames or longer from a typical cell. Quantitative statistical studies that combine data from many cells are not a good way to investigate vesicle-to-vesicle heterogeneity because the mean frame-to-frame step length varies by a factor of 2 or more among cells plated in the same dish. Here, we focus primarily on specific trajectories from three different cells and a detailed statistical analysis of 37 trajectories from a single representative cell.

A gallery of high-resolution trajectories showing three apparently different behaviors is presented in Figure 2 as two-dimensional projections. Below, we will classify the vesicles as "immobile", "mobile", and "directed-motion" vesicles, corresponding to parts a−c of Figure 2, respectively. Some vesicles jiggle within seeming traps or "cages" for several seconds (Figure 2a). These trapped vesicles tend to be the brightest; that is, traps seem more common very close to the PM. Frequently, these vesicles migrate, either rapidly or slowly, among a succession of such traps. For vesicle #4, we show the same trajectory with every 20th point plotted to illustrate the loss of detail that occurs when sampling at only 2 Hz. Other vesicles sample space widely; seldom move in long, straight segments; and largely avoid traps or cages (Figure 2b). Finally, a small minority of vesicles, perhaps 5%, move very rapidly along smooth, quasi-linear paths (Figure 2c). Next, we discuss the motion in detail.

Heterogeneity among Vesicles. Force-free random walks tend to sample local space thoroughly before slowly moving to a substantially different region.[26] Short samples of free random walks vary widely in the shape and range of their trajectories.[20,27−29] In treating single-particle tracking data, we must address the question of whether the observed motion could have been produced with reasonable probability by a particular

random walk model (e.g., free diffusion, diffusion within a compartment, diffusion within a radial potential, and diffusion among obstacles) with one set of model parameters. If so, the motion is *homogeneous.* If multiple models or sets of parameters are required to encompass the observed behavior, then the motion is *heterogeneous*. We distinguish *heterogeneity across vesicles* (vesicles moving differently from each other) from *heterogeneity within single trajectories* (a single vesicle changing its "state of motion" with time). The latter is more difficult to demonstrate. Vesicles may differ from each other in local environment or in the number of attached motor proteins, for example. For individual vesicles, motor activity may stop and start; the vesicle may bind to a site and then release; the vesicle may diffuse into a region of substantially different viscoelastic properties; or the local actin cortex may reorganize.

While it is conceivable that the "trapped" trajectories of Figure 2a and the directed motion of Figure 2c might arise from force-free random walks, it is highly unlikely. One way to assess this possibility uses the closed-form expression for the probability that a free walk in three dimensions with diffusion constant D remains entirely within a sphere of radius R_0 for time $\tau = n\Delta t$.[30] To test the trapped trajectories, we set $\Delta t = 0.0262$ s and $D = 0.0044\ \mu\text{m}^2/\text{s}$, from the mean one-step diffusion coefficient for the immobile group (defined below). The probability that a walk remains in a sphere with a radius of 50 nm for $n = 20$ steps is 2.2×10^{-4}; it falls to 2.6×10^{-10} and to 6.1×10^{-40} for $n = 50$ and 200, respectively. Thus, the compact, 300−500-step trajectories (e.g., vesicles #1, 2, and 4) are surely not free random walks. We can also show that the small subtraps of 20−100 steps probably arise from a real restoring force or confinement rather than a free random walk that happens to remain localized. The probability of remaining within a sphere of radius $R_0 = 25$ nm is 2.2×10^{-4} for $n = 5$ and only 3.1×10^{-16} for $n = 20$. To analyze the directed segments of Figure 2c, we take $D = 0.0074\ \mu\text{m}^2/\text{s}$, the mean for the mobile group (defined below). The longer and faster a quasi-linear segment, the less likely that it would occur in a random walk. At a typical contour speed of 1500 nm/s (Figure 2c), the particle moves a net distance of 200 nm in 5 steps (400 nm in 10 steps). The probability that a random walk *exits* a sphere of that radius in that amount of time is 2.4×10^{-4} (1.1×10^{-8}). Thus, a 5-step quasi-linear segment at 1500 nm/s might arise from random motion in a data set as large as ours, but a 10-step segment at the same speed is highly improbable. Segments moving 10 steps at only 700 nm/s have a probability of 0.029, which is likely to occur in a large data set. However, there is a substantial margin of safety in assuming these trajectories are primarily due to directed motion, since they all achieve *several* such improbable quasi-linear segments within the *same* trajectory.

In Figure 3a, we show the scatter plot of three-dimensional mean-square displacements (MSD(τ) values) for 37 well-isolated individual trajectories from a single cell. Each MSD(τ) datum is the average over the complete trajectory of all measurement intervals with the same lag time, $\tau = n\Delta t$:

$$\text{MSD}(\tau = n\Delta t) = \frac{1}{(N-n)}\sum_{i=1}^{N-n}[(x_{i+n} - x_i)^2 + (y_{i+n} - y_i)^2 + (z_{i+n} - z_i)^2] \quad (1)$$

Here, the frame interval is $\Delta t = 0.0262$ s, N is the total number of frames in the trajectory, and for each n the sum runs over all possible intervals of length $\tau = n\Delta t$. The single-vesicle MSD(τ) plots typically increase monotonically for τ up to about half the total trajectory length and then may increase or decrease rapidly depending on the peculiarities of each trajectory. The heavy black line in the figure shows ⟨MSD(τ)⟩, the mean of all single-vesicle MSD(τ) values. This *vesicle-averaged* quantity is different from the average over all frame-to-frame steps of all vesicles, which would weight vesicles with 500-frame trajectories 10 times more heavily than vesicles with 50-frame trajectories at small t.

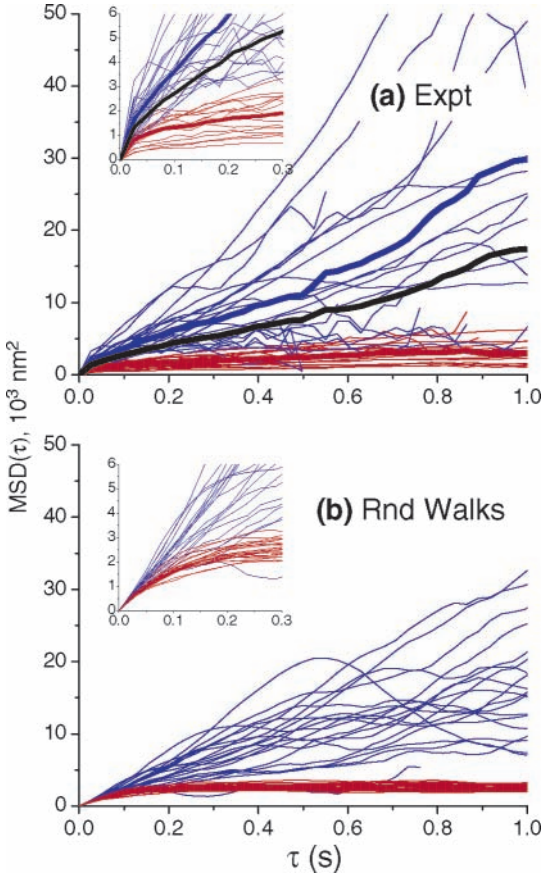

Figure 3. (a) Experimental single-vesicle MSD(τ) plots for 37 vesicles (thin lines) from a single representative cell. Color shows division into the mobile group (blue) and the immobile group (red). Bold lines show the vesicle-averaged ⟨MSD(τ)⟩ for the mobile group (blue), the immobile group (red), and all 37 vesicles combined (black). (b) Same as part a but for 25 free random walks of 50 frames each from a model with $D = 0.0074\ \mu\text{m}^2/\text{s}$ (blue lines) and for 25 random walks in a parabolic restoring potential with $D = 0.0044\ \mu\text{m}^2/\text{s}$ and force constant $\kappa = 0.009$ pN/nm (red lines).

For comparison, Figure 3b shows the same type of scatter plot for 50-frame free random walks (blue curves) and for 200-frame walks in a parabolic restoring potential (red curves). We chose 50 and 200 frames as representatives of the duration of the more mobile and less mobile trajectories. The experimental distribution of MSD($n\Delta t$) at each value of n is much broader than that from a particular free random walk model. That is the signature of substantial heterogeneity across vesicles.

To characterize the heterogeneity more quantitatively, in the inset of Figure 4, we pool and bin frame-to-frame step lengths, $r_i = ((x_i - x_{i+1})^2 + (y_i - y_{i+1})^2 + (z_i - z_{i+1})^2)^{1/2}$, from all trajectories except the directed ones and plot the distribution $P(r)$. Trajectories longer than 50 frames were truncated at 50 to avoid strong overweighting. For free diffusion of a homogeneous population of vesicles in three dimensions with diffusion coefficient D, the distribution would be

$$P(r; n\Delta t) = Ar^2 e^{-r^2/4Dn\Delta t} \quad (2)$$

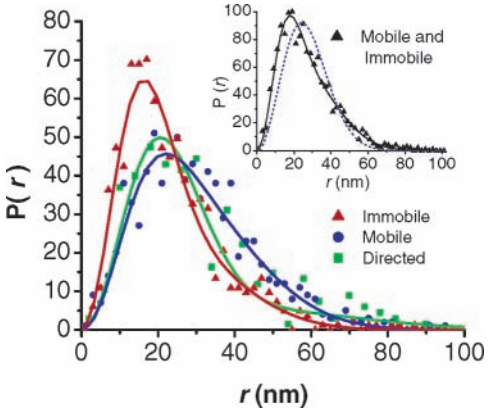

Figure 4. Probability distribution for pooled frame-to-frame step lengths, r's, for the immobile, mobile, and directed-trajectory groups of vesicles from the same cell as that in Figure 2, with $\Delta t = 0.0262$ s between frames. The mobile and immobile trajectories were truncated at 50 frames each to avoid gross overweighting of long trajectories. Solid lines are least-squares fits to the sum of two distributions of the form of eq 2. Fits to a single diffusion coefficient are poor in each case. Inset: $P(r)$ for the combined mobile and immobile groups showing the best one-component fit ($D_1 = 0.0053$ μm^2/s) and two-component fit (solid line, $D_1 = 0.0023 \pm 0.0002$ μm^2/s, $A_1 = 0.83$, $D_2 = 0.0080 \pm 0.0004$ μm^2/s, $A_2 = 0.17$). See Table 1 and text for fitting details.

with A being a normalization constant.[31] We carried out a nonlinear least-squares fit of the data to this function with $n = 1$; each bin is weighted as N_i^{-1}, appropriate for a Poisson distribution with the mean and variance equal to N_i, the number of counts in bin i.[32] The fitting results are given in Table 1. For the complete data set, the fit to eq 2 is poor (Figure 4, inset, dashed line), as judged by the reduced chi-square statistic $\chi_\nu^2 = 3.2$ (the probability is $\ll 10^{-3}$ that χ_ν^2 would be so large by chance). The data are well fit by a sum of *two* such distributions with the diffusion coefficients $D_1 = 0.0023$ μm^2/s and $D_2 = 0.0082$ μm^2/s; now, $\chi_\nu^2 = 0.83$ ($p = 0.7$, which is reasonable). We have similarly fit the distribution of squared displacements, r^2 values, and the distributions of projections of steps Δx, Δy, and Δz to the appropriate functions for free diffusion. One-component fits are again poor, and two-component fits again succeed. In all cases, the best-fit values of D_1 and D_2 are consistent with the two-component fits to $P(r)$. These fitting results confirm the existence of heterogeneity among vesicles on the shortest time scale sampled, 0.0262 s. For $n = 10$ ($n\Delta t = 0.262$ s), the $P(r)$ and $P(r^2)$ distributions are again not well fit by a single diffusion coefficient ($\chi_\nu^2 = 3.9$). Thus, the heterogeneity persists at $t = 0.262$ s and longer.

Having established heterogeneity among vesicles, we next divide the vesicles into two groups labeled *mobile* and *immobile* according to whether the MSD(0.157 s) is greater or less than 2300 nm^2. This yields 22 mobile and 15 immobile vesicles for this representative cell. The division is shown by color in Figure 3a. It represents an attempt to find two groups of vesicles each of which is reasonably well described by a single random walk model, the immobile group by a confined random walk and the mobile group by force-free diffusion. Any such sharp division is somewhat arbitrary, since the outcomes of random walks from a single model vary widely for trajectories of 25−500 steps. Plots of vesicle-averaged $\langle \mathrm{MSD}(\tau) \rangle$ for the two groups are shown in Figure 3a. For the mobile group, $\langle \mathrm{MSD}(\tau) \rangle$ is fairly linear at long times up to 1 s, although negative curvature is evident in the first few steps (inset). For the immobile group, $\langle \mathrm{MSD}(\tau) \rangle$ shows strong negative curvature in the first few steps but does not saturate even on a time scale of 5 s.

In Figure 4, we compare pooled frame-to-frame step length distributions, $P(r)$, for $n = 1$ across three groups of vesicles: mobile, immobile, and directed. For the five directed trajectories, all steps were pooled in order to obtain a reasonably smooth histogram; the diffusive motion at the end of trajectory #D1 was excluded. The mobile and immobile groups have overlapping but substantially different distributions of r even at the shortest time sampled. A one-step diffusion coefficient computed directly from the data as $\langle r^2 \rangle / 6\Delta t$ differs by a factor of 1.7 for the groups: $D_{1-\mathrm{step}} = 0.0074$ μm^2/s for the mobile group and 0.0044 μm^2/s for the immobile group. By the 40th step ($\tau = 1$ s), the $\langle \mathrm{MSD} \rangle$ values of the two groups differ by a factor of 5. Perhaps surprisingly, $P(r)$ for the five directed trajectories is not very different from that of the immobile group and the mobile group, although the directed trajectories do exhibit a somewhat longer tail at large r.

Importantly, even after dividing the trajectories into mobile and immobile groups, heterogeneity remains within each group (Table 1). That is, each group's $P(r)$ for $n = 1$ remains too broad to be well fit by a single component. For the one-component fits, χ_ν^2 is 1.37 for the mobile group ($p = 0.05$) and 1.60 for the immobile group ($p = 0.01$). The two-component fits to the mobile and immobile groups yield acceptably low values of χ_ν^2 and give essentially the same values for the two diffusion coefficients D_1 and D_2 for the two groups within the fitting uncertainty. The mobile and immobile groups differ primarily in their relative weighting of the fast and slow components, which will be important in our interpretation below.

We also searched for *orientational* correlation between successive steps on the theory that directed motion along quasi-linear tracks would cause a preferred orientation to persist in time. For each trajectory, we computed the n-frame velocity autocorrelation function:[21]

$$G(n) = \frac{1}{(N-n)\langle r^2 \rangle} \sum_{i=1}^{N-n} (\mathbf{r}_i \cdot \mathbf{r}_{i+n}) \qquad (3)$$

where $\mathbf{r}_i$ is the frame-to-frame three-dimensional displacement vector measured from frame i to frame $i + 1$ and $\langle r^2 \rangle$ is the mean-square displacement over the entire trajectory. $G(n)$ measures the correlation in the orientation of pairs of frame-to-frame steps spaced by n frames. For a free random walk, $G(n)$ drops from 1 at $n = 0$ to zero (within the noise) for all successive n because the steps are uncorrelated in direction.

As shown in Figure 5, in the immobile group, the vesicle-averaged $\langle G(n) \rangle$ value dips to -0.31 ± 0.09 (one standard deviation) at $n = 1$, perhaps remains slightly negative for $n = 2-3$, and then fluctuates about zero. Within the immobile group, all individual trajectories show significantly negative $G(1)$ values. For the mobile group, $\langle G(n) \rangle$ dips to -0.17 ± 0.13 (one standard deviation) at $n = 1$, which appears to be significantly negative beyond the noise level. Only half of the individual trajectories from the mobile group exhibit significantly negative $G(1)$ values. The group of five directed trajectories shows $\langle G(n) \rangle$ values that remain substantially *positive* over at least 15 frames, in contrast to the mobile and immobile groups. This is consistent with directed motion along quasi-linear tracks (Figure 2c) that persists on average for ~0.3 s.

Especially for nearly stationary vesicles, random measurement error or apparatus vibration might contribute significantly to the negative values of $G(1)$. To test this possibility, we measured 500 displacements from 19 different vesicles within *fixed cells*. The apparent motion is a superposition of measurement error, apparatus vibration, and genuine thermal motion, so it sets an

TABLE 1: Fits of Distributions of Frame-to-Frame Displacements, $P(r)$, for Different Vesicle Groups[a]

vesicle group[a]	A_1	D_1 (μm^2/s)	A_2	D_2 (μm^2/s)	% fast [b]	χ_ν^2 [c]
mobile + immobile (one)	0.47(2)	0.0053(1)				3.2
mobile + immobile (two)	0.76(6)	0.0023(2)	0.15(2)	0.0082(3)	0.57	0.83
mobile (one)	0.181(10)	0.0068(2)				1.37
mobile (two)	0.21(3)	0.0028(8)	0.089(19)	0.0087(4)	0.70	0.85
immobile (one)	0.37(2)	0.0036(1)				1.60
immobile (two)	0.52(4)	0.0022(2)	0.050(16)	0.0075(6)	0.37	0.70

[a] Vesicle groups as defined in text. The trajectories are truncated at 50 steps to avoid overweighting of long trajectories. Nonlinear least-squares fits to the function $P(r;\Delta t) = \sum_{j=1}^{2} A_j r^2 e^{-r^2/4D_j\Delta t}$, with $\Delta t = 0.0262$ s; the fitted parameters are A_j and D_j. The fits labeled (one) and (two) include one and two components of D_j, respectively. Each bin is weighted as N_i^{-1}, appropriate for a Poisson distribution with the mean and variance equal to N_i, the number of counts in bin i. [b] Fraction of steps arising from the faster component at D_2 according to the fit. Note that this differs from $A_2/(A_1 + A_2)$ because the two components have different "widths" in $P(r)$. [c] Reduced chi-square statistic for each fit.

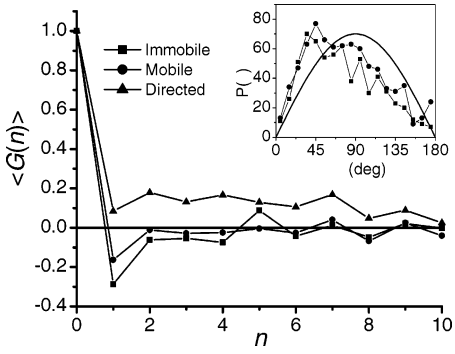

Figure 5. Vesicle-averaged $G(n)$, the n-step velocity autocorrelation function (eq 3) averaged over each group (immobile, mobile, and directed-motion trajectories) including all steps. Inset: Distribution of angles, θ's, between two successive steps for immobile and immobile groups as indicated; $\theta = 0$ means the two velocities are antiparallel. The solid line shows the sin θ distribution expected for a free random walk.

upper bound on the possible contribution of random error to $G(1)$ for the mobile and immobile vesicles. For the fixed cells, we find $\langle r^2\rangle = 165$ nm^2 and $\langle G(1)\rangle = -0.5$, that is, the average over vesicles of the mean dot product $\langle\langle \mathbf{r}_i\cdot\mathbf{r}_{i+1}\rangle\rangle \approx \langle r^2\rangle\langle G(1)\rangle = -82.5$ nm^2. For comparison, the immobile vesicles have $\langle r^2\rangle = 790$ nm^2 and $\langle G(1)\rangle = -0.31 \pm 0.09$, yielding $\langle\langle \mathbf{r}_i\cdot\mathbf{r}_{i+1}\rangle\rangle \approx -240 \pm 70$ nm^2; the mobile vesicles have $\langle r^2\rangle = 1580$ nm^2 and $G(1) = -0.17 \pm 0.13$, yielding $\langle\langle \mathbf{r}_i\cdot\mathbf{r}_{i+1}\rangle\rangle \approx -270 \pm 200$ nm^2. The average *relative* contribution of measurement error and vibration to $\langle \mathbf{r}_i\cdot\mathbf{r}_{i+1}\rangle$ is evidently 30% at most. The negative values of $G(1)$ are evidently dominated by real motion at least for the immobile vesicles, and probably for the mobile vesicles as well.

We also measured the distribution of angles, $P(\theta)$, between successive steps (inset of Figure 5), with θ defined as 0° for antiparallel steps. For a random walk with no correlation between successive directions, $P(\theta) = {}^1/_2 \sin\theta$, which peaks at 90°. Both vesicle groups show substantial and comparable "backward peaking", consistent with negative $G(1)$ values.

Dependence of $\langle r^2\rangle$ on z. Part of the heterogeneity among vesicles is apparently due to the increase in local $\langle r^2\rangle$ with increasing z. In Figure 6a, we truncate trajectories at 50 frames and pool single steps to plot $\langle D_{3D}\rangle = \langle r^2\rangle/6\Delta t$ versus *apparent* z for the mobile group, the immobile group, and the two groups combined. Here, $\langle D_{3D}\rangle$ is the mean of individual steps. The truncation avoids the effects of photobleaching. The range of r^2 values contributing to each $\langle D_{3D}\rangle$ point is very large. $\langle D_{3D}\rangle$ increases exponentially with increasing apparent z; the increase is a factor of 10 for each 225 nm. Analogous plots of the mean two-dimensional diffusion constant in the xy plane, $\langle D_{xy}\rangle$ versus z, and of the mean one-dimensional diffusion constant along z, $\langle D_z\rangle$ versus z, are also exponential and have essentially the same slope. There is no evidence that the motion in the xy plane is different from the motion along z.

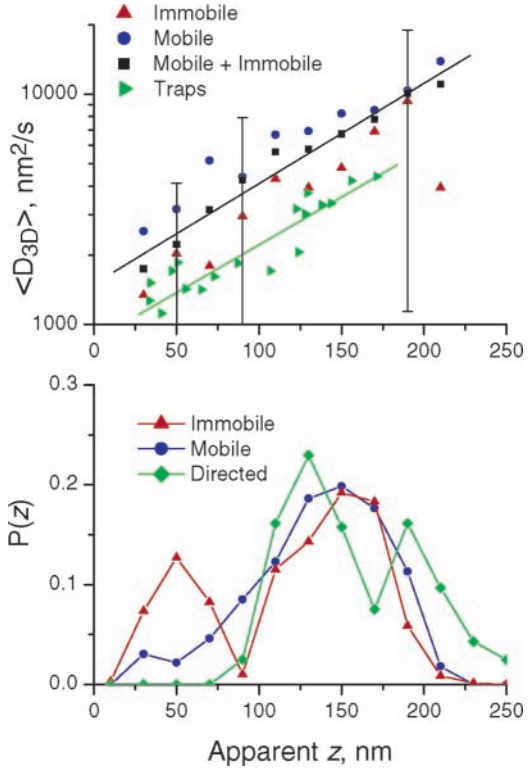

Figure 6. (a) Dependence of the one-step, three-dimensional diffusion coefficient on *apparent* relative z. (The data are not corrected for the variation of intrinsic brightness of vesicles.) Each $\langle D_{3D}\rangle$ is the mean over all single steps occurring within a small range of z for one cell (black), for the immobile group (red), and for the mobile group (blue). Long trajectories were truncated at 50 frames to minimize the effects of photobleaching and to minimize overweighting of long trajectories. The brightest intensity observed defines $z = 0$. The solid line is a least-squares fit to the combined mobile + immobile data. $\langle D_{3D}\rangle$ increases a factor of 10 over a 225-nm change in apparent z. The vertical bars show one standard deviation of data contributing to each point. The trap data (green) are best-fit model D values from walks within a parabolic restoring potential plotted against the mean apparent z for each trap (see Table 1 and text). (b) Distribution of apparent z for the mobile, immobile, and directed-motion groups averaged over all vesicles. Long trajectories truncated as above.

Recall that the distribution of intrinsic vesicle brightness makes detailed interpretation of intensity as directly related to z inappropriate for individual vesicles. However, here, we seek trends in averages over many trajectories. In the earlier chromaffin study,[21] dispersion in the GFP copy number broadened the distribution of $\langle D_z\rangle$ at each z but affected the

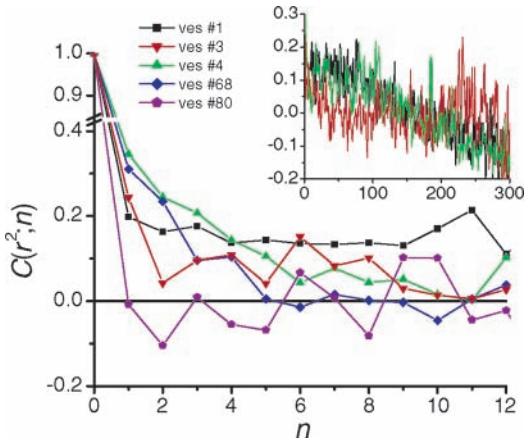

Figure 7. Time-correlation function of $r^2(t)$ for individual vesicles as labeled. See eq 4 for the definition of $C(r^2; n)$. The persistence of positive $C(r^2; n)$ indicates prolonged periods of above-average r^2 compared with a free random walk. Inset: $C(r^2; t)$ for immobile vesicles #1, 3, and 4 over 300 frames.

slope of the log plot very little. The z dependence in PC12 cells is milder than that in chromaffin cells, for which $\langle D_z \rangle$ increased a factor of 10 for each 130-nm increase in z.

Figure 6b shows histograms of the apparent z locations sampled by the mobile and immobile groups, again with steps pooled from only the first 50 frames of each trajectory to avoid photobleaching effects. The peak at $z = 50$ nm for the immobile group is dominated by the four brightest vesicles in the whole cell (vesicles #1−4; see Figure 2a). These are the same vesicles that carry out sequential visits among small traps. Other immobile vesicles and the directed-motion vesicles evidently sample a similar range of z as the mobile group.

Heterogeneity within Single Trajectories. Some changes in the single-vesicle state of motion are fairly obvious to the eye. The directed-motion vesicles of Figure 2c pause, change speed, and change direction; trajectory #D1 changes from directed motion to more diffusive motion like that of the mobile group. The immobile vesicles at low apparent z jump quickly or migrate slowly among small mini-traps with a diameter of ~50 nm or less. Other vesicles evidently change their diffusion coefficient ($\langle r^2 \rangle$) in subtle ways. A useful test of memory in $r^2(t)$ that averages out much of the noise is the time-correlation function:[33,34]

$$C(r^2; n) = ((N-n)^{-1}\sum_{i=1}^{N-n}(\delta r^2)_i(\delta r^2)_{i+n})/(N^{-1}\sum_{i=1}^{N}(\delta r^2)_i^2) \quad (4)$$

Here, $(\delta r^2)_i = (r^2)_i - \langle r^2 \rangle$ measures positive and negative fluctuations of r^2 about its mean value calculated over the entire trajectory. N is the number of steps in the trajectory. The denominator normalizes $C(r^2; n)$ to 1 at $n = 0$. If during the trajectory r^2 persistently takes on values that are larger than average (or smaller than average) over the time range $\tau = n\Delta t$, then the average of the product of the fluctuations will be nonzero and $C(r^2; n)$ will remain positive (or negative) over n frames. For free random walks, $r^2(t)$ has no memory from frame to frame, so $C(r^2; n)$ decays immediately to the noise level at $n = 1$.

As shown in Figure 7, $C(r^2; n)$ exhibits diverse behavior. Among the mobile group, we find examples such as vesicles #16, 27, and 68 for which $C(r^2; n)$ remains positive over 3−10 frames (75−260 ms). Evidently, these vesicles have short periods of above-average r^2 that persist longer than such periods in free random walks. $C(r^2; n)$ is not seriously affected by deleting any particular short run of 5−10 frames. Thirteen of the 22 mobile vesicles (59%) have $C(r^2; n = 1) > 0.1$. To test the statistical significance of this result, we ran 10 000 force-free random walks with a distribution of step lengths that mimics that observed in the mobile group so that the noise level is representative of that in the real data. Only 18% of these walks had $C(r^2; n = 1) > 0.1$, so the observed effect is significant. Positive $C(r^2; n)$ could signal a transient increase in diffusion constant or engagement and disengagement of a motor protein from the actin cortex. In contrast, vesicle #80 and many others have $C(r^2; n)$ that decays to zero within the noise at $n = 1$, like a free random walk. Visual inspection of trajectories #68 and 80 in Figure 2b shows how $C(r^2; n)$ discerns correlations not readily detected by the eye. If motor activity led primarily to stretches of *quasi-linear motion* with longer-than-average step lengths, we might expect both $C(r^2; n)$ and the velocity autocorrelation function, $G(n)$, to remain *positive* for similar periods, but this is not observed.

For vesicles #1, 3, and 4 from the immobile group, $C(r^2; n)$ remains positive in the range 0.10−0.35 at $n = 1$. Most of the vesicles from the immobile group behave similarly. This may be related to the strong negative values of $G(1)$ exhibited by the immobile group, as if long "second displacements" tend to reverse direction from long "first displacements". The model random walks with restoring potential (see below) capture some of this behavior, predicting $C(r^2; n = 1) = 0.06-0.13$.

Beyond $n = 1$, vesicles #1 and 4 show $C(r^2; n)$ that decreases *slowly* and nearly linearly from positive to negative values over 300 frames (inset of Figure 7). Several other vesicles from the immobile group exhibit this behavior. Vesicle #3 shows $C(r^2; n)$ that gradually sags below zero and then rises above zero. Vesicles #1 and 4 sample a series of traps whose physical properties differ in a way captured by $C(r^2; n)$. Evidently, the traps vary in size, local diffusion coefficient, or elasticity. To see how this causes $C(r^2; n)$ to *decrease* linearly, suppose there were only two traps, one favoring larger-than-average values of r^2 and the other favoring smaller-than-average values of r^2. At small time lags, $C(r^2; n)$ multiplies values of r^2 by other values within the same trap, so that a positive δr^2 value tends to be multiplied by a positive δr^2 value and a negative δr^2 value tends to be multiplied by a negative δr^2 value, causing $C(r^2; n)$ to remain positive. As the lag time increases to delay times comparable to the dwell time within traps, positive δr^2 values are more often multiplied by negative δr^2 values and $C(r^2; n)$ gradually decreases. At sufficiently large n, positive δr^2 values will be multiplied primarily by negative δr^2 values and $C(r^2; n)$ goes negative. If the time sequences of the large-r^2 and small-r^2 traps were reversed, $C(r^2; n)$ would still *decrease* monotonically from positive to negative values. A sequence of traps of gradually increasing (or decreasing) local average r^2 behaves the same. $C(r^2; n)$ plots that "sag" in the middle (e.g., vesicle #3, inset of Figure 7) occur when the local average of r^2 varies slowly but in *non*-monotonic fashion, as in a period of positive δr^2 followed by a period of negative δr^2 followed by another period of positive δr^2. Long negative−positive−negative sequences give the same result.

Mechanical Model of "Mini-Traps". Close inspection of the immobile trajectories often reveals sequential visits to a series of *smaller* regions with a diameter of ~50 nm or less, separated by 50−200 nm in space. Good examples are vesicles #1 and 4 in Figure 2. The calculations presented above under "Random Walk Models" show that it is highly unlikely that force-free random walks would remain so confined for so long.

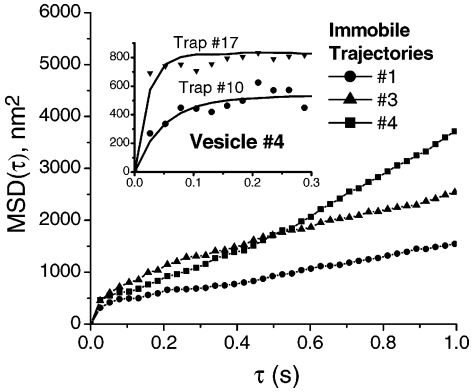

Figure 8. (a) For immobile vesicles #1, 3, and 4, MSD(τ) averaged over the entire trajectory. Inset: MSD(τ) for two individual traps sliced from trajectory #4 (Figure 2). The solid lines are the best fits to the model of a random walk in a parabolic radial restoring potential. See Table 1 for the best-fit parameters.

Most of these mini-traps are roughly spherical. The transition between two smaller regions often occurs as a rapid, 50−100-ms "jump", after which the vesicle dwells in the next small region for 0.5−1 s or more. We believe this motion is *not* caused by the thermal drift of the entire sample relative to the microscope. If it were, we would expect other slow-moving vesicles to show correlated drift in the same *xy* direction during the same movie frames, but this does not occur. If the mini-traps were fixed locations in space, the vesicles might visit a mini-trap, move on to another mini-trap, and later revisit the first mini-trap. This does not seem to occur.

For vesicle #4, the MSD(τ) plot averaged over the entire trajectory (Figure 8) is a composite of two types of motion. After an abrupt initial step up, it exhibits mild *positive* curvature over 1 s. On that time scale, the vesicle has made several abrupt migrations among traps substantially displaced in space. The MSD(t) plots for immobile vesicles #1 and 3 also take a similar sharp initial step up. In the range 0−1 s, the MSD for vesicle #1 subsequently grows *linearly*, while the MSD for vesicle #3 shows *negative* curvature. Such plots are quite sensitive to the distribution of mini-trap durations and the distances between mini-traps; they do not faithfully report on the size and viscoelastic properties of the mini-traps themselves.[29,35−37]

To extract quantitative information about the traps themselves, we excised individual localized segments of trajectories #1 and 4, as judged by the eye, for comparison with confined random walk models. These vary in length from 20 to 150 frames. The MSD(n) plots for individual localized traps saturate at long times and are thus appropriate for analysis as confined random walks (Figure 8, inset). In modeling such data as a walk within a restoring potential or confined to a sphere, we need a procedure for finding the model parameters that best fit the MSD(τ) data. First, we fit the data to a function of the form $\mathrm{MSD}(\tau) = A\tau^2/(B + \tau^2)$, with A and B being adjustable parameters chosen in a least-squares sense. We generate 10 000-step walks with various combinations of parameters (D and κ or D and R_0) chosen on a grid that covers the range required by the range of trap MSD(τ) data. For each parameter pair, the MSD(τ) was generated from the corresponding random walk. We found that the potential parameter κ (or R_0) can be obtained directly from the high-τ asymptote of MSD(τ) from the equation $\kappa = 6kT/A$ (or $R_0 = (0.86A)^{1/2}$). The microscopic diffusion coefficient, D, depends on both the asymptote and the initial slope. We fit D to a function of the form $D = a_1 + a_2(A/B) + a_3(A/B)^2 + a_4(A/B)^3$, with ($D$, A/B) pairs generated from 10 000-step walks. These equations allow us to find the best random walk model

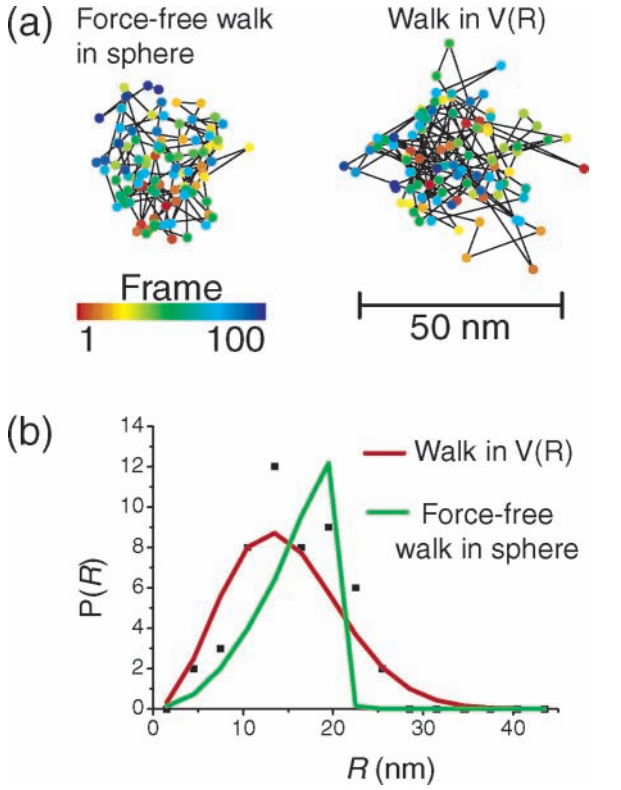

Figure 9. (a) Two confined random walks projected onto a plane. Each walk was tuned to fit MSD(τ) for trap #10 in Table 1. On the left-hand side: walk within a sphere. On the right-hand side: walk within a restoring potential. (b) $P(R)$ experimental distribution for trap #10. The solid lines are model $P(R)$ for the walk within a restoring potential and the walk within a sphere that best fit the experimental MSD(τ) data. The χ_ν^2 statistic is 3 times lower for the walk within a restoring potential, 0.89 vs 2.48.

parameters directly from single-trap MSD(τ) data. Using the best combination of D and κ (or D and R_0), we generate a 10 000-step walk whose MSD(τ) closely fits the experimental data by design. Those results provide the speed distribution, $P(r)$, the time-correlation function, $C(r^2; n)$, and the velocity autocorrelation function, $G(n)$, for further tests of the validity of the model.

As described above, we have modeled the data with two different types of random walks: force-free walks confined within a sphere and walks with a central restoring potential of $V(R) = {}^1/_2\kappa R^2$, with R being the distance from the center of force. Figure 9 contrasts *xy* projections of 100-step walks within a sphere and with a restoring potential using the parameters that best fit MSD(τ) for a particular trap, trap #2. The force-free walk fills the sphere uniformly, while the restoring potential model concentrates points near the center of force and allows a softer "edge" to the distribution.

For the restoring potential model, the inset of Figure 8 shows best fits to MSD(τ) for two traps from trajectory #4, one small and the other large. In both cases, the model fits both the rising portion and the asymptote, including the sharp step upward at $n = 1$. Importantly, the restoring force model tuned to fit MSD(τ) also fits experimental $P(R)$ quite well ($\chi_\nu^2 = 0.89$). It appears that we are cutting segments of essentially homogeneous motion from a full trajectory which is heterogeneous. For sufficiently long walks, we have $P(R) = AR^2 \exp(-{}^1/_2\kappa R^2/kT)$, the canonical ensemble. The model predicts negative $G(n = 1)$ values in qualitative accord with experiment, but the magnitude is 20−40% too small. In the model, negative $G(n)$ values persist to $n = 3$−4. This is not easy to see in noisy, single-trap data.

TABLE 2: Properties of 17 Traps Fit to a Random Walk Model with Restoring Potential

vesicle # (trap #)	duration of trap (frames)	mean apparent z (nm)	best-fit force constant, κ,[a] (pN/nm)	best-fit D[a] (μm^2/s)	$D_{1-\text{step}}$[b] (μm^2/s)
#1 (#1)	36	33	0.049	0.0010	0.0013
#1 (#2)	21	34	0.050	0.0020	0.0015
#1 (#3)	42	41	0.034	0.0008	0.0011
#1 (#4)	45	47	0.050	0.0019	0.0017
#2 (#5)	48	51	0.026	0.0012	0.0019
#1 (#6)	67	56	0.044	0.0010	0.0014
#4 (#7)	71	65	0.036	0.0009	0.0014
#1 (#8)	84	73	0.037	0.0010	0.0016
#1 (#9)	62	87	0.031	0.0008	0.0018
#4 (#10)	50	107	0.047	0.0018	0.0017
#1 (#11)	20	123	0.037	0.0065	0.0032
#4 (#12)	98	124	0.045	0.0016	0.0021
#1 (#13)	67	128	0.030	0.0035	0.0030
#71 (#14)	53	129	0.023	0.0033	0.0037
#1 (#15)	50	138	0.036	0.0057	0.0033
#72 (#16)	69	156	0.023	0.0036	0.0042
#4 (#17)	151	171	0.029	0.0064	0.0044

[a] D is the short-time model diffusion coefficient; κ is the restoring force constant in the model potential $V(R) = {}^1/_2\kappa R^2$. See text for further explanation. Estimated accuracy of ±30% for D and ±15% for κ. [b] Calculated from single-trap MSD($t = 0.0262$ s) as $D_{1-\text{step}} = \text{MSD}/6t$.

However, $G(n)$ values averaged both over all the immobile vesicles (Figure 4) and over the pooled trap data (not shown) hint at such persistence. The average over all mobile vesicles does not. The model also predicts the positive first step of the time-correlation function, $C(r^2; n)$, for traps, although only at ~50% of the experimental value.

Model walks confined to a sphere with no restoring potential can be tuned to fit MSD(τ) and $G(n)$ just as well as the walks with restoring potential (fits not shown). However, these walks fill the sphere uniformly (Figure 9), that is, $P(R) = AR^2$, which gives a qualitatively incorrect shape compared with experiment. The fit to $P(R)$ is quantitatively poor, with the χ_ν^2 value being typically 3 times larger than that for the restoring potential model. The data clearly support an elastic model of the medium surrounding the vesicle.

The best-fit parameters from restoring force models for 17 mini-traps are collected in Table 2. The short-time diffusion constant, D, varies from 0.0008 to 0.0065 μm^2/s. The force constant, κ, varies from 0.023 to 0.050 pN/nm. Taking account of both the fitting error for single-trap data and the variation in outcomes for short trajectories from a single motional model, we estimate that D is accurate to ±30% and κ is accurate to ±15%. Thus, the apparent heterogeneity in parameters among mini-traps is real. Small D correlates with large κ. There is substantial variation of both D and κ with apparent z, in the direction that D increases and the traps become less stiff as the distance from the PM increases. The fitted values of D for each trap are plotted in Figure 6 as a function of the mean value of z within the trap. The data generally track the trend of $\langle D_{3D} \rangle$ versus z for the entire immobile group.

Discussion

Comparisons with Previous Work. Several excellent studies have tracked LDCV motion in PC12 cells and chromaffin cells,[18,21,38−41] including the effects of F-actin stabilizing and destabilizing drugs and of differentiation with nerve growth factor (NGF). A landmark PC12 study[5] with a 0.8-Hz frame rate and a 50-nm spatial resolution observed a few vesicles that moved in a directed manner over micrometer distances, many that moved randomly, and many that remained stationary within the measurement accuracy. However, no stationary vesicles were observed to start moving, and only one rapidly moving vesicle was observed to stop. That study also stained the actin cortex, measured its thickness to be at least 390 nm, revealed filamentous actin within the cortex, and directly observed its remodeling on a time scale of tens of seconds. A recent detailed study of LDCVs in the processes of PC12 cells differentiated with NGF found a broad distribution of one-step mean-square displacements (at $\tau = 0.5$ s), quite similar to that observed here for undifferentiated cells.[20] Under the assumption that each vesicle has a particular, *time-invariant* diffusion coefficient, the existence of a *distribution* of diffusion coefficients was demonstrated by a rigorous statistical analysis. In addition to demonstrating such vesicle-to-vesicle heterogeneity on much shorter time and length scales, our study reveals heterogeneity within a subset of single-vesicle trajectories.

An earlier 3D tracking study of chromaffin cells with a 5−10-nm resolution[18] focused on the motion of vesicles just prior to docking. Mobile vesicles evolved into docked vesicles, which preferentially exocytosed upon stimulation. The docked vesicles, which lie closer to the PM than mobile vesicles, sampled mini-traps quite similar in radius (24 ± 9 nm) to those we describe here for PC12 cells. As in the present work, vesicles were observed to change states from mobile to immobile and back again. PC12 and chromaffin cells seem quite similar with regard to many details of vesicle motion. We have avoided calling the immobile vesicles *docked* (which suggests readiness for exocytosis), since there is evidence that in PC12 cells the *mobile* vesicles are more likely to carry out exocytosis immediately after depolarization than the immobile vesicles.[12]

Motor-Dominated Motion. A dual-motor transport system evidently operates in chromaffin cells[42] and neurons,[4,43] and a trimotor system operates in melanocytes.[4,8] Vesicles are transported from the trans-Golgi network (TGN) to the actin cortex by kinesin walking on microtubules (MTs). The melanocytes also harbor dynein motors that transport them from the cortex back to the TGN. Recent work showed that, in PC12 cells, kinesins transport immature LDCVs from the Golgi to the actin cortex via MTs and suggested that myosin-Va is involved in tethering and subsequent motion of mature vesicles on a shorter length scale within the cortex.[10,11] The directed-motion trajectories of Figure 2c are almost surely dominated by motor activity. On the basis of known mean speeds of motors in vitro, most of these trajectories seem to involve kinesin walking on MTs. Kinesin is a processive motor which takes 8-nm steps with a dwell time on the order of 5 ms between steps. It moves at a mean speed on the order of 1500 nm/s,[44] consistent with the most typical segment speeds in Figure 2c. Under our conditions, such motion should create a trajectory of fairly uniform local speed with frame-to-frame displacements on the order of 40 nm. This is consistent with the appearance of many of the short segments of the directed-motion trajectories. The directed-motion vesicles are never among the brightest vesicles (Figure 6), indicating that the purported microtubules lie some 100−300 nm above the PM.

The wide variability in local speed (460−2200 nm/s) could arise from the presence of different types of kinesins or dyneins on the same motor or from changes in the local degree of viscous drag due to the variation of F-actin density or morphology. In addition, the melanosome study[8] showed that functional myosin-Va on a *kinesin*-driven vesicle may impede progress by transient binding to F-actin as it streams by, causing the local speed to

vary in time and space. The stall force of kinesin is 5−8 pN,[44] twice as large as the stall force for myosin-V[45] and much larger than the restoring force of the observed mini-traps (∼1 pN at extension $R = 25$ nm). Kinesin thus wins in competition with myosin-V and also would readily pull LDCVs through mini-traps of the size and strength measured near the PM.

Most of the directed segment speeds are too fast for average speeds of myosin-V, which lie in the range 200−500 nm/s.[44] However, the frame-to-frame $P(r)$ distribution for the directed-motion group (Figure 3) shows a small fraction of displacements in the range 50−80 nm, which may be more consistent with myosin-V motion, as described below. The backtracking behavior might be due to the added presence of dynein on the same vesicle, although there is no biochemical evidence at the present time for dyneins on LDCVs.

Capture and Assisted Diffusion. Myosin-Va is bound to at least 50% of the large dense-core secretory vesicles (LDCVs) of PC12 cells.[10,11] What is its purpose? In the "capture model" that evolved from the melanosome study,[8] myosin-Va *at least* plays the role of concentrating melanosomes in the actin cortex by binding them to F-actin. For both melanosomes and LDCVs, such transient binding can explain the steady-state preponderance of vesicles in the cortex relative to the rest of the cell. Within the actin cortex itself, vesicle binding to F-actin via myosin-Va would also cause the vesicle density to mimic the density of F-actin binding sites, although other mechanisms for docking such as SNARE complexes at the PM must be considered as well.

Myosin-Va should *walk* on F-actin unless it is subject to an unknown regulation mechanism. Strong evidence for active transport within the cortex comes from two studies that expressed a dominant negative tail fragment of myosin-Va lacking the motor domains. This construct blocks normal vesicle−myosin-Va binding. In both mouse melanocytes[8] and PC12 cells,[11] this depleted the frame-to-frame step length distribution, $P(r)$, at the high end. The depleted range was about 0.1−0.3 μm/s for melanocytes and 0.28−0.8 μm/s for PC12, roughly comparable to myosin-V average speeds in vitro (0.2−0.5 μm/s).[44] Neither study found evidence of directed motion with a spatial resolution of ∼50 nm and frame rates of 1−2 Hz, which would average over several 80-ms dwell periods between motor steps, as detailed below.

Additional evidence consistent with motor-driven active transport of the mobile group comes from the effects on vesicle motion of F-actin disruption or stabilization by drugs in undifferentiated PC12 cells.[5] LDCV diffusive motion *slowed* when the actin cortex was degraded by latrunculin and *stopped completely* when the remodeling of F-actin was prevented by phalloidin or the withdrawal of MgATP.[5] Almers and co-workers suggested that F-actin provides tracks for active transport but a rigidified actin cortex is too stiff and has pore sizes too small to allow even diffusive transport to occur.

One of our goals in this high-resolution work was to look closely for short segments of directed, myosin-driven motion. While positive $C(r^2; n = 1)$ in the mobile group could be caused by brief periods of processive motor activity interspersed with periods of local diffusion, *directed* motion is not in evidence. There are a modest number of quasi-linear segments in the mobile trajectories, but they are neither longer nor more frequent than the seemingly directed segments that appear in a free random walk. It seems highly unlikely that still better temporal and spatial resolution would reveal directed motion.

The best model for the motion of the *mobile* LDCVs in the actin cortex evidently involves motor-assisted transport, also known as *assisted diffusion*, within a viscoelastic medium. Myosin-Va intermittently binds the LDCVs to the actin cortex and enhances transport by dragging the vesicles along cross-linked, entangled F-actin filaments. Our observation of subdiffusion on a 100-ms time scale and the absence of significant directed motion in our high-resolution trajectories constrain this model severely. The apparently diffusive motion must be due to the complexity of the actin meshwork itself. Recent in vitro studies of myosin-V at 25 °C and excess ATP concentration revealed 37-nm steps and average dwell times of 80 ms between steps, yielding an average speed of ∼500 nm/s.[45] If the mesh size of the F-actin network is ∼50 nm, with a high density of cross-links and branches, *most* steps might transfer myosin-V to another filament. If the power stroke is fast and successive steps along the same quasi-linear filament are rare, directed motion will not be observed and the motion will appear diffusive even at a high resolution.

Our spatial and temporal resolution can resolve individual steps and dwell periods (26-ms resolution vs 80-ms mean dwell time). Thus, the mobile group's $P(r)$ may be a composite of two modes of motion on the 25-ms time scale: longer, motor-assisted frame-to-frame displacements (primarily the fast component; see Figure 4 and Table 1) interspersed with shorter displacements during dwell times (primarily the slow component). The fast and slow components overlap significantly, so our statements can be only semiquantitative. The slow component has frame-to-frame displacements primarily in the range 5−30 nm; only 25% of this distribution has $r > 20$ nm. We suggest it arises from periods in which the vesicles move thermally within a viscoelastic medium unassisted by motor action; such motion may involve confinement within "holes" of the actin network and tethering to F-actin by a myosin-V motor. We draw this inference from the similarity between the minority, slow component of $P(r)$ of the mobile group and the majority, slow component of the immobile group (Table 1). The length of the tail region of myosin-Va is ∼30 nm, so wagging or bending motions of the tail and its cargo can explain the 5−30-nm range of displacements. This motion cannot simply involve jiggling of the LDCV about a fixed position but rather must involve motion of the center of gravity of the vesicle for ∼25 ms, perhaps accommodated by local adjustment of F-actin.

The fast component of $P(r)$ for the mobile group (Table 1) has frame-to-frame displacements primarily in the range 10−60 nm; only 25% of the fast distribution has $r < 20$ nm. We suggest that these displacements primarily involve a *superposition* of myosin-V-driven motion with thermal motion of the vesicle on its tether. It is not easy to estimate the distribution of measured displacements for a vesicle carrying one myosin-V when exactly one of the two frames catches a motor step. Steps that cross over to another F-actin strand can be substantially shorter than 37 nm. In addition, when a myosin-V step occurs near the middle of a camera frame, its effect will be distributed roughly equally across *two* frame-to-frame displacements (involving three successive frames). A single 37-nm step thus sometimes contributes 15−20 nm of directed motion to two successive displacements. This further shortens the measured active displacements. It may also contribute to positive values of $C(r^2; n = 1)$. Thermal motion of the LDCV on its tether will further broaden the distribution of displacements by perhaps ±15 nm, the range of observed displacements within the slow component. In summary, we estimate that a *pair* of frames that catches exactly one active motor step will yield measured displacements primarily in the range ∼15−45 nm, which covers most of the range of the fast component of $P(r)$.

While most of the fast component of $P(r)$ for the mobile group can be reasonably well understood in terms of single crossover steps of a myosin-V motor, two factors subtly hint at the presence of two or more active motors on at least some of the mobile vesicles. First, the mean dwell time of 80 ms combined with a duty factor for binding to F-actin that is <1 predicts that <30% of the frames will catch a motor step, while the fast component of $P(r)$ contributes 70% of the displacements (Figure 4). A two-motor LDCV should take steps more frequently than a one-motor LDCV. Second, ~20% of the mobile group displacements fall in the range 45−70 nm, somewhat longer than that expected for single myosin-V steps. This may be due to double steps within a frame. For only one active motor per vesicle, we estimate the probability of two steps within a single frame to be ~4%. Two motors acting independently would double this probability and help explain the substantial fraction of very long steps.

If the mobile group undergoes tethered diffusion like the immobile group when its motors are dwelling between steps or disengaged from F-actin entirely, a reasonable corollary is that the immobile group *lacks actively walking motors or has fewer active motors*. Do the immobile vesicles completely lack myosin-Va? Competitive binding of the dominant negative tail region of myosin-Va to LDCVs severely depletes their concentration in the cortex. This suggests that intact myosin-Va is the transient binding agent that concentrates LDCVs in the actin cortex and that the immobile vesicles harbor myosin-Va. If so, our interpretation further suggests that the myosin-Va motors on immobile vesicles are less numerous or are subject to a regulatory mechanism that alters motor activity but not binding to F-actin. The observed changes in the state of vesicle motion within single trajectories supports this hypothesis of regulated motor activity. Changes in the state of motion might also help explain the substantial fast component of $P(r)$, which contributes 0.4 of the frame-to-frame displacements of the immobile group. Regulation of motor activity might be related to the concept of mobile and immobile *pools* of vesicles whose state changes in response to cell stimulation and the rate of exocytosis. Alternatively, all myosin-Va may be active all of the time, but the immobile vesicles harbor only one myosin-Va, while mobile vesicles harbor two or more. We cannot distinguish these possibilities by imaging the vesicles alone.

Microrheology. From the viewpoint of the field of rheology, the actin cortex is a dense solution of entangled, semiflexible polymer rods cross-linked by other proteins such as α-actinin, filamin, and spectrin. In this context, our vesicle tracking experiment is a one-particle microrheology experiment. Here, we compare our results for LDCV motion in the actin cortex of PC12 cells with earlier microrheology experiments on anionic (carboxylated) fluorescent microspheres embedded in entangled F-actin solutions in vitro[46,47] and in the cytoplasm of live Swiss 3T3 fibroblast cells.[48] Weitz and co-workers[47] tracked spheres with a radius of $a = 0.23-0.42$ μm in F-actin solutions with a rod length of ~15 μm and a mesh size of $\xi = 0.3$ μm. The smallest spheres had $a/\xi \sim 0.8$. These spheres exhibit anomalous subdiffusion with MSD $\sim \tau^{0.6}$ at short times and significant *negative* curvature on a log−log plot (Figure 10), consistent with slow permeation of the spheres through the network. Spheres with only slightly higher values of a/ξ, ~1.1 and ~1.4, remain caged; that is, the MSD reaches a plateau related to the mesh size and elasticity for $\tau > 0.1$ s. An earlier study[46] at a lower F-actin density ($\xi \sim 1$ μm) found free diffusion for particles with $a/\xi = 0.15$ ($a = 0.15$ μm, MSD $\sim \tau^1$) and anomalous subdiffusion for particles with $a/\xi = 1.4$ ($a = 1.4$ μm, MSD $\sim \tau^{0.73}$, again with slight negative curvature of the log−log plot). The in vitro work demonstrates the extreme sensitivity of the motion to the ratio a/ξ, analogous to the sensitivity of diffusion to the density of obstacles as the percolation limit is approached.

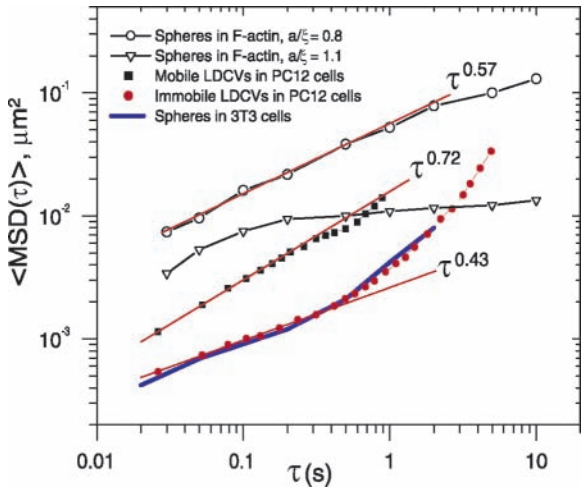

Figure 10. Comparison of ⟨MSD(τ)⟩ for microspheres in F-actin solution (data from ref 47, ratio of sphere radius to mesh size, a/ξ, of 0.8 for open circles and 1.1 for open triangles); for mobile and immobile LDCVs in PC12 cells (present work, filled squares and circles, respectively); and for microspheres with $a = 50$ nm injected into Swiss 3T3 cells (blue line, data from ref 48). The thin red lines show various power-law slopes as indicated.

Perhaps the most detailed view of the actin cortex comes from recent electron tomography images of *Dictyostelium* cells.[49] These reveal actin filaments of 100−500 nm in length with many branches and cross-links. Open spaces among the rods have dimensions on the order of 50 nm, which is the mesh size, ξ, typically cited for the actin cortex. The local density of actin filaments varies substantially in space on a ~0.3−0.5-μm scale. In PC12 cells adhered to glass, Almers and co-workers[5] stained the F-actin to reveal crisscrossing filaments interpreted as actin bundles at the base of the cell. These bundles measured 1−5 μm in length, and about half the bundles were observed to move on a 1-min time scale or less. The mini-traps examined here have diameters <50 nm, consistent with a mesh size of $\xi \sim 50$ nm within the actin cortex. To explain the observed fwhm of our Gaussian fitting functions, we must convolve a 120-nm fwhm Gaussian (representing the real LDCV size) with the point-spread function of the microscope. An LDCV radius of $a \sim 60$ nm is consistent with results from electron microscopy,[50] so we estimate $a/\xi \sim 1.1$ in our study. The in vitro work suggests we should observe anomalous subdiffusion and caging of the LDCVs.

The mobile group exhibits MSD $\sim \tau^{0.7}$ at short times (Figure 10), more similar to the short-time limit of Weitz's *smaller* spheres having $a/\xi \sim 0.8$, for which MSD $\sim \tau^{0.6}$, than to expectations for $a/\xi \sim 1.1$. Less confinement of the mobile LDCVs than what is expected can be taken as further evidence of motor-assisted diffusion.

In contrast, the immobile group of LDCVs indeed seem caged at short times, and the log−log plot shows MSD $\sim \tau^{0.4}$ at short times, quite similar to the short-time behavior of Weitz's intermediate-sized and large spheres having $a/\xi \sim 1.1$ and 1.4 (Figure 10). This is consistent with the possibility that the immobile LDCVs lack active motors. However, at longer times, the LDCV log−log plot exhibits *positive* curvature, which is qualitatively different from the behavior of microspheres in entangled actin filaments in vitro. This positive curvature arises

from the "jump diffusion" observed for many of the immobile vesicles, as described above. Such behavior is reminiscent of the 2D "diffusion by hops" of a variety of integral membrane proteins within the PM of erythrocytes, [36] although it occurs on much longer time scales.

The cause of these 3D jumps within the actin cortex is uncertain. They are most evident among the immobile vesicles with smallest apparent *z*. The similarity between mini-trap size and the ~50-nm mesh size of the actin cortex suggests jumps between holes in the mesh, possibly assisted by F-actin remodeling events. Within the large trap at the end of trajectory #4 (Figure 2a), the physical environment of the vesicle seems to tighten up as a function of time over ~0.5 s, without substantial change in location of the vesicle center-of-mass. This suggests local remodeling of the surrounding F-actin in response to a jump by the vesicle.

Remarkably, in their study of anionic fluorescent spheres of $a = 50$ nm microinjected into the cytoplasm of Swiss 3T3 cells, Wirtz and co-workers[48] obtained log−log MSD(τ) plots *quantitatively similar* to ours for the immobile group, including the unusual positive curvature (Figure 10). This similarity between inert microspheres in vivo and the immobile LDCVs suggests the occurrence of jump diffusion due to remodeling of actin in both cases. However, the comparison is between LDCVs embedded in the actin cortex of PC12 and spheres distributed throughout 3T3 cells. Moreover, there is some evidence of directed motion of the microspheres, which would also contribute to positive curvature in the log−log plot.

Conclusion

This high-resolution tracking study of LDCVs within the actin cortex of PC12 cells reveals interesting new quantitative details of the vesicle motion. A better understanding of the factors causing the heterogeneity observed here requires the measurement of high-resolution vesicle trajectories *simultaneously* with images of other labeled components, such as F-actin, the motor proteins kinesin and myosin-Va, and SNARE complexes. This may be most feasible using cracked cells, which give biochemical access to the actin cortex and associated vesicles and proteins.

Acknowledgment. J.C.W. dedicates this paper to Tom Baer, an esteemed colleague and friend whose enthusiasm for and curiosity about science (and life and red wine) are always infectious. Daniel Axelrod kindly provided the prototype of our vesicle tracking program. We thank Meyer Jackson, Gerard Marriott, Arun Yethiraj, and Jim Skinner for many stimulating discussions. This research was supported in part by the National Science Foundation (CHE-0071458), by the University of Wisconsin Alumni Research Foundation, and by the UW-Madison Department of Chemistry.

References and Notes

(1) Alberts, B.; Johnson, A.; Lewis, J.; Raff, M.; Roberts, K.; Walter, P. *Molecular Biology of the Cell*, 4th ed.; Garland Science: New York, 2002.
(2) Sund, S. E.; Axelrod, D. *Biophys. J.* **2000**, *79*, 1655.
(3) Rose, S. D.; Lejen, T.; Casaletti, L.; Larson, R. E.; Pene, T. D.; Trifaro, J. M. *J Neurochem.* **2003**, *85*, 287.
(4) Langford, G. M. *Traffic* **2002**, *3*, 859.
(5) Lang, T.; Wacker, I.; Wunderlich, I.; Rohrbach, A.; Giese, G.; Soldati, T.; Almers, W. *Biophys. J.* **2000**, *78*, 2863.
(6) Vale, R. D. *Cell* **2003**, *112*, 467.
(7) Wu, X. S.; Rao, K.; Zhang, H.; Wang, F.; Sellers, J. R.; Matesic, L. E.; Copeland, N. G.; Jenkins, N. A.; Hammer, J. A., III. *Nat. Cell Biol.* **2002**, *4*, 271.
(8) Wu, X.; Bowers, B.; Rao, K.; Wei, Q.; Hammer, J. A., III. *J. Cell Biol.* **1998**, *143*, 1899.
(9) Wu, X.; Bowers, B.; Wei, Q.; Kocher, B.; Hammer, J. A., III. *J. Cell Sci.* **1997**, *110* (Pt 7), 847.
(10) Rudolf, R.; Salm, T.; Rustom, A.; Gerdes, H. H. *Mol. Biol. Cell* **2001**, *12*, 1353.
(11) Rudolf, R.; Kogel, T.; Kuznetsov, S. A.; Salm, T.; Schlicker, O.; Hellwig, A.; Hammer, J. A., III; Gerdes, H. H. *J. Cell Sci.* **2003**, *116*, 1339.
(12) Han, W.; Ng, Y. K.; Axelrod, D.; Levitan, E. S. *Proc. Natl. Acad. Sci. U.S.A.* **1999**, *96*, 14577.
(13) Steyer, J. A.; Almers, W. *Nat. Rev. Mol. Cell Biol.* **2001**, *2*, 268.
(14) Axelrod, D. *Traffic* **2001**, *2*, 764.
(15) Ng, Y. K.; Lu, X. H.; Levitan, E. S. *J. Physiol. (London)* **2002**, *542*, 395.
(16) Han, W.; Li, D.; Levitan, E. S. *Ann. N.Y. Acad. Sci.* **2002**, *971*, 627.
(17) Oheim, M.; Loerke, D.; Chow, R. H.; Stuhmer, W. *Philos. Trans. R. Soc. London, Ser. B* **1999**, *354*, 307.
(18) Oheim, M.; Stuhmer, W. *Eur. Biophys. J.* **2000**, *29*, 67.
(19) Burke, N. V.; Han, W.; Li, D.; Takimoto, K.; Watkins, S. C.; Levitan, E. S. *Neuron* **1997**, *19*, 1095.
(20) Ng, Y. K.; Lu, X.; Gulacsi, A.; Han, W.; Saxton, M. J.; Levitan, E. S. *Biophys. J.* **2003**, *84*, 4127.
(21) Johns, L. M.; Levitan, E. S.; Shelden, E. A.; Holz, R. W.; Axelrod, D. *J. Cell Biol.* **2001**, *153*, 177.
(22) Axelrod, D. *J. Biomed. Opt.* **2001**, *6*, 6.
(23) Yildiz, A.; Forkey, J. N.; McKinney, S. A.; Ha, T.; Goldman, Y. E.; Selvin, P. R. *Science* **2003**, *300*, 2061.
(24) Ghosh, R. N.; Webb, W. W. *Biophys. J.* **1994**, *66*, 1301.
(25) Cheezum, M. K.; Walker, W. F.; Guilford, W. H. *Biophys. J.* **2001**, *81*, 2378.
(26) Berg, H. C. *Random Walks in Biology*; Princeton University Press: Princeton, NJ, 1993.
(27) Saxton, M. J. *Biophys. J.* **1993**, *64*, 1766.
(28) Saxton, M. J. *Biophys. J.* **1993**, *64*, 1053.
(29) Saxton, M. J. *Biophys. J.* **1994**, *66*, 394.
(30) Rubin, R. J.; Mazur, J.; Weiss, G. H. *Pure Appl. Chem.* **1976**, *46*, 143.
(31) Crank, J. *The Mathematics of Diffusion*; Oxford University Press: Oxford, U.K., 1956.
(32) Bevington, P. R.; Robinson, D. K. *Data Reduction and Error Analysis for the Physical Sciences*, 3rd ed.; McGraw-Hill: New York, 2003.
(33) Chandler, D. *Introduction to Modern Statistical Mechanics*; Oxford University Press: Oxford, U.K., 1987.
(34) Yang, H.; Xie, X. S. *J. Chem. Phys.* **2002**, *117*, 10965.
(35) Kusumi, A.; Sako, Y.; Yamamoto, M. *Biophys. J.* **1993**, *65*, 2021.
(36) Tomishige, M.; Kusumi, A. *Mol. Biol. Cell* **1999**, *10*, 2475.
(37) Saxton, M. J. *Biophys. J.* **1995**, *69*, 389.
(38) Steyer, J. A.; Horstmann, H.; Almers, W. *Nature* **1997**, *388*, 474.
(39) Steyer, J. A.; Almers, W. *Biophys. J.* **1999**, *76*, 2262.
(40) Ng, Y. K.; Lu, X.; Watkins, S. C.; Ellis-Davies, G. C.; Levitan, E. S. *J. Neurosci.* **2002**, *22*, 3890.
(41) Ryan, T. A. *Proc. Natl. Acad. Sci. U.S.A.* **2003**, *100*, 2171.
(42) Rose, S. D.; Lejen, T.; Casaletti, L.; Larson, R. E.; Pene, T. D.; Trifaro, J. M. *Ann. N.Y. Acad. Sci.* **2002**, *971*, 222.
(43) Stafford, P.; Brown, J.; Langford, G. M. *Biol. Bull.* **2000**, *199*, 203.
(44) Howard, J. *Mechanism of Motor Proteins and the Cytoskeleton*; Sinauer Associates, Inc.: Underland, MA, 2001.
(45) Rief, M.; Rock, R. S.; Mehta, A. D.; Mooseker, M. S.; Cheney, R. E.; Spudich, J. A. *Proc. Natl. Acad. Sci. U.S.A.* **2000**, *97*, 9482.
(46) Amblard, F.; Maggs, A. C.; Yurke, B.; Pargellis, A. N.; Leibler, S. *Phys. Rev. Lett.* **1996**, *77*, 4470.
(47) Gardel, M. L.; Valentine, M. T.; Crocker, J. C.; Bausch, A. R.; Weitz, D. A. *Phys. Rev. Lett.* **2003**, *91*, 158302.
(48) Tseng, Y.; Kole, T. P.; Wirtz, D. *Biophys. J.* **2002**, *83*, 3162.
(49) Medalia, O.; Weber, I.; Frangakis, A. S.; Nicastro, D.; Gerisch, G.; Baumeister, W. *Science* **2002**, *298*, 1209.
(50) Tooze, S. A.; Flatmark, T.; Tooze, J.; Huttner, W. B. *J. Cell Biol.* **1991**, *115*, 1491.